Proceedings of ASME Turbo Expo 2010: Power for Land, Sea and Air
GT2010
June 14-18, 2010, Glasgow, UK

GT2010-22061

SECONDARY FLOW REDUCTION BY BLADE REDESIGN AND ENDWALL CONTOURING USING AN ADJOINT OPTIMIZATION METHOD

Jiaqi Luo*, Juntao Xiong and Feng Liu
Department of Mechanical and Aerospace Engineering
University of California, Irvine, CA92697-3975
* Visiting Student from Department of Fluid Mechanics
Northwestern Polytechnical University, Xi'an, China
Email: jiaqil@uci.edu

Ivan McBean
Alstom Power (Switzerland)
Baden, Switzerland

ABSTRACT

For low-aspect-ratio turbine blades secondary loss reduction is important for improving performance. This paper presents the application of a viscous adjoint method to reduce secondary loss of a linear cascade. A scalable wall function is implemented in an existing Navier-Stokes flow solver to simulate the secondary flow with reduced requirements on grid density. The simulation result is in good agreement with the experimental data. Entropy production through a blade row is used as the objective function in the optimization of blade redesign and endwall contouring. With the adjoint method, the complete gradient information needed for optimization can be obtained by solving the governing flow equations and their corresponding adjoint equations only once, regardless of the number of design parameters. Three design cases are performed with a low-aspect-ratio steam turbine blade tested by Perdichizzi and Dossena. The results demonstrate that it is feasible to reduce flow loss through the redesign of the blade while maintaining the same mass-averaged turning angle. The effects on the profile loss and secondary loss due to the geometry modification of stagger angle, blade shape and endwall profile are presented and analyzed.

NOMENCLATURE

a	Speed of sound
A_i	Jacobian matrices, $A_i = \frac{\partial f_i}{\partial W}$
B	Boundaries of ξ domain
c_p	Constant pressure specific heat
D	The computational domain (ξ domain)
f_j	Inviscid flux
f_{vj}	Viscous flux
I	Cost function
k	Turbulent kinetic energy; Thermal conductivity
K_{ij}	Transformation functions between the physical domain and the computational domain, $K_{ij} = \frac{\partial x_i}{\partial \xi_j}$
n_i	Unit normal vector in the ξ domain, pointing outward from the flow field
N_j	Unit normal vector in the physical domain, pointing outward from the flow field
R	Flow equations
s	Entropy, $s = c_p(\frac{1}{\gamma} ln\frac{p}{p_1} - ln\frac{\rho}{\rho_1})$, p_1 and ρ_1 are references
s_{gen}	Entropy generation per unit mass flow rate
u_i	Velocity components
u_τ	Friction velocity
W	Conservative flow variables, $W = \{w_1, w_2, w_3, w_4, w_5\}^T$
$\overline{\beta}$	Mass-averaged exit flow turning angle
δy	Distance from the first grid point away from wall boundary to the solid wall
Λ	Weight of the penalty function
ν	Kinematic viscosity, $\nu = \frac{\mu}{\rho}$, μ is viscosity
ω	Dissipation rate
Ψ	Co-state variables, Ψ=$\{\psi, \phi_1, \phi_2, \phi_3, \theta\}^T$
τ_w	Wall shear stress
ξ_i	Coordinates in the computational domain

INTRODUCTION

At present, further performance improvement of turbomachinery is difficult through traditional design procedures because significant efficiency gains have already been obtained. However, with the fast growth of computational power and advances in numerical methods, Computational Fluid Dynamics (CFD) coupled with advanced optimization algorithms provides a new cost-effective way to improve and optimize turbomachinery design as compared to classical methods based on manual iteration. Many design optimization approaches such as response surface methodology [1, 2], genetic algorithms [3] and finite difference methods [4] were applied in design development.

A flow solver which can support physically accurate flow solutions is required in the optimization design based on CFD. Not all turbulence models can sufficiently model complex flow. Wilcox gave an overview of turbulence models in his paper [5] and demonstrated that the models based on the ω equation can support satisfactory solutions for many flows. In this paper, the flow solutions are obtained by using the turbomachinery flow code *Turbo*90 in which the *k*-ω SST turbulence model and a third-order Roe scheme are used.

In the past several decades, research has been done to improve the efficiency of flow solvers. However, to maintain high accuracy of turbulent flow solution, a fine mesh with a large number of grid points is needed. Kalitzin [6] and Shih [7] proposed the use of wall-functions and applied them to flat-plate flow and turbomachinery flow. By using wall functions, the boundary layer can be resolved with a relatively coarse mesh. In this paper, a scalable wall function is implemented to correct the skin friction on the wall and to update the turbulent kinetic energy and dissipation rate in the *k*-ω SST turbulence model.

In the turbulent flow with low Mach number of a low-aspect-ratio turbine blade, the flow loss may be categorized as profile loss and secondary loss. In a rather low aspect ratio blade, the secondary flow can influence the entire flow field along the spanwise direction. The theory of secondary flow was described in Horlock's paper [8] and much experimental work was done by Perdichizzi and Dossena [9–12]. The effects of exit Mach number, incidence flow angle, pitch-chord ratio, endwall contouring and stagger angle are investigated. Subsequently, Koiro [13] and Hermanson [14] presented simulation and validation of the effects on the secondary flow at different flow conditions and geometry based on CFD. The geometry of a blade row can be modified to reduce the pressure gradient in the pitchwise direction and consequently suppress the cross flow. The area ratio and exit flow angle of a blade row can be influenced by a change of stagger angle. Contoured endwall profile will accelerate or decelerate the flow in the axial direction and change the pressure gradient in the pitchwise direction. All these changes influence the secondary vortex generation, and consequently the secondary flow features of the blade row.

Besides the flow solver, an important component in a typical Aerodynamic Design Optimization (ADO) problem is the optimizer. Because of its high efficiency in calculating the gradient information needed in the optimization procedure, much research work has been done on the adjoint approach advocated by Jameson [15, 16]. It has been widely used in the aerodynamic design optimization for airfoils, wings, and wing-body configurations [15–18]. However, there are only a few published applications to turbomachinery design optimization based on the adjoint method [19–24]. Following previous success of an adjoint optimization method using the Euler equations for a three-dimensional turbine blade by the present authors [24], a continuous viscous adjoint method is adopted in this paper. With the adjoint method, the gradient information can be obtained by solving the Navier-Stokes equations and their corresponding viscous adjoint equations only once, regardless the number of design parameters.

The present paper reports the redesign of a linear turbine blade row by three different approaches: (1) restagger of the blade profile in the spanwise direction; (2) combination of the restagger and blade profile modification; and (3) end-wall contouring. The cost function is defined as the sum of the entropy generation per unit mass flow rate and a penalty function used to enforce the constraint of constant turning angle of the flow. The formulations of the objective function, constraints, and design parameters are presented The different boundary conditions and the gradient formulae are derived and presented for the Navier-Stokes equations. The effects of stagger angle, blade shape and endwall profile on secondary flow are discussed.

VALIDATION OF THE FLOW SOLVER

In a fully-turbulent flow, the boundary layer can be subdivided into three layers, a viscous sublayer, a buffer layer and a logarithmic layer. The logarithmic layer plays an important role in the mixing process. The wall shear stress cannot be computed accurately with a finite-difference scheme unless the first grid point away from the wall is within the viscous sublayer. To remove such a stringent requirement on the computational grid, one may make use of the log law of the velocity profile as expressed below to compute the wall shear stress u_τ instead of using direct finite-differencing of the velocity.

$$u^+ = \frac{U}{u_\tau} = \frac{1}{\kappa} log(y^+) + B \tag{1}$$

$$y^+ = \frac{u_\tau \delta y}{\nu} \tag{2}$$

where κ is the von Karman constant, B is a constant related to the roughness of the wall, and δy is the distance from the wall.

Eqn. (1) is implicit for u_τ for a given flow velocity U at the point $y = \delta y$. Solution for u_τ may encouter difficulties in convergence. Eqn.(1) becomes singular at separation points where the velocity U approaches zero. For the above reason, the standard wall function is not particularly practical. Following the same implementation as in the commercial CFX solver, one can use an alternative velocity scale u^* instead of u^+ in the definition of y^+:

$$u^* = \sqrt{a_1 k} \tag{3}$$

$$y^* = \frac{\rho u^* \delta y}{\mu} \tag{4}$$

$$y^+ = max(y^*, 11.06) \tag{5}$$

where a_1 is 0.31 and k is the turbulence kinetic energy away from the wall. The above y^+ is then used in the log law to calculate u_τ explicitly

$$u_\tau = \frac{U}{\frac{1}{\kappa} log(y^+) + B} \tag{6}$$

The wall shear stress is then determined as

$$\tau_w = \rho u^* u_\tau \tag{7}$$

This is the so-called scalable wall function. In a fully-turbulent flow, the turbulent kinetic energy is never zero in the flow domain away from the wall and thus by applying Eqn.(6) the friction velocity u_τ can be calculated even U approaches zero. Eqn.(5) indicates that should the calculated y^+ fall into the viscous sublayer, it is restricted to the lower limit of the log region.

The corrected skin friction partly depends on the turbulent kinetic energy as shown in Eqn.(3). Following Prandtl's assumption for the turbulent viscosity

$$\nu_t = \kappa u_\tau \delta y \tag{8}$$

k and ω can be updated and the wall functions for k and ω are specified as

$$k = \frac{u_\tau^2}{a_1}, \quad \omega = \frac{u_\tau}{a_1 \kappa \delta y} \tag{9}$$

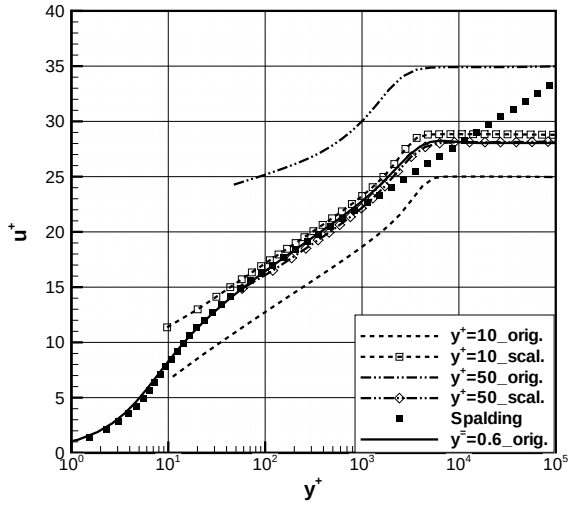

Figure 1. VELOCITY PROFILES FOR THREE DIFFERENT GRIDS

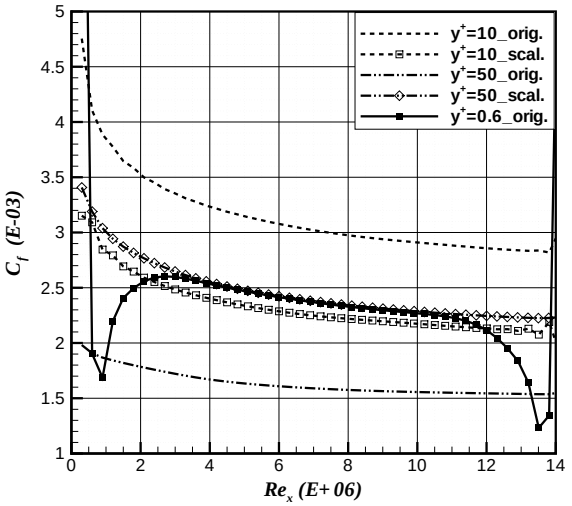

Figure 2. SHEAR STRESS DISTRIBUTIONS FOR THREE DIFFERENT GRIDS

A. Demonstration of the Wall Function in Flat-Plate Flow

In order to validate the applicability of the scalable wall function, the flow over a flat plate is tested first. Here the flow calculations are performed with three different grids, $y^+ = 0.6$, $y^+ = 10$, and $y^+ = 50$, respectively.

Figure 1 presents the computed velocity profiles at the 50 percent axial location of the wall along with Spalding's formula. The suffix *orig* denotes solutions without the use of the wall func-

Table 1. Cascade geometric data

Chord length	55.2 mm
Axial chord	34.0 mm
Blade height	50.0 mm
Stagger angle	39.9 deg
Inlet blade angle	76.1 deg

tion. Figure 2 presents the skin friction distributions along the wall. The predicted velocity profiles on the grids with $y^+ = 10$ and $y^+ = 50$ with the wall function agree well with Spalding's formula as well as that computed on the fine grid with $y^+ = 0.5$ without the wall function. The shear stress distributions computed by the method with the wall function also match well with that computed on the fine grid without the wall function. Those computed on the coarse grids without the wall function, however, deviates significantly from the log law and the result on the fine grid. These results show that with the aid of the wall function, the velocity profile and the wall shear stress can be correctly modeled even on rather coarse grids.

B. Simulation of Secondary Flow of a Cascade Blade

The test case for design optimization in this paper is the subsonic linear cascade investigated experimentally by Perdichizzi and Dossena [9, 10]. The isentropic exit Mach number is 0.7. The geometry data of the blade are shown in Table 1.

The flow solution is calculated with the k-ω SST turbulence model and a third-order Roe scheme. As shown in Perdichizzi's paper [9], the local kinetic energy loss coefficient can be defined as:

$$\zeta = \frac{\left(p_{s(y,z)}/p_{t2(y,z)}\right)^{\frac{\gamma-1}{\gamma}} - \left(p_{s(y,z)}/p_{t1(y,z)}\right)^{\frac{\gamma-1}{\gamma}}}{1 - \left(\bar{p}_{sMS}/\bar{p}_{t1MS}\right)^{\frac{\gamma-1}{\gamma}}} \qquad (10)$$

where the subscript MS denotes mid-span, p_{t1} and p_{t2} denote the total pressure at inlet and exit respectively, p_s denotes static pressure at exit, and the bar indicates mass-averaging. The secondary loss in the spanwise direction is defined as the difference between the mass-averaged kinetic energy loss on each spanwise section and that on the mid-span.

Four different grids are studied, with the grid density of $144\times40\times48$, $200\times40\times48$, $144\times80\times96$ and $144\times120\times144$, respectively. Computations on the first three grids included the use of the wall function, whreas no wall function is used on the fourth grid, which is extremely fine and is assumed to resolve to the wall. Figure 3 presents the mass-averaged total pressure from inlet to exit. Figure 4 presents the secondary loss distributions in the spanwise direction. Table 2 presents the calculated

Table 2. Calculation results on four grids

Grids	1	2	3	4
p_0	0.98244	0.98279	0.98316	0.98290
β (deg)	75.1739	75.2530	75.1463	75.1397
ζ_0 (%)	3.66809	3.59117	3.39072	3.46764
ζ_p (%)	1.85672	1.82411	1.61873	1.67342
ζ_s (%)	1.81137	1.76706	1.77199	1.79422

results where p_0, β, ζ_0, ζ_p and ζ_s denote total pressure, flow turning, total loss, profile loss and secondary loss, respectively. The computed profile loss is close to the experimental value of about 1.75. However, the secondary loss is less than the experimental value of about 2.35. Despite this difference in absolute value, the computations on the four grids demonstrate an acceptable level of grid convergence of the solutions with the wall function. The optimization studies in the following part of this paper are performed on the first grid in order to save computational time.

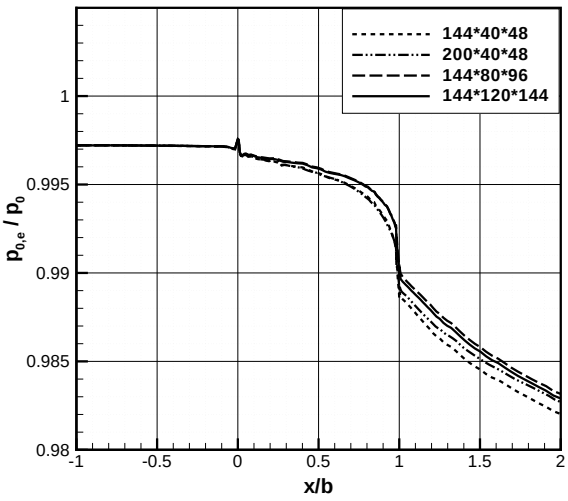

Figure 3. MASS-AVERAGED TOTAL PRESSURE FROM INLET TO EXIT

VISCOUS ADJOINT EQUATIONS

The implementation of the adjoint method was described previously for the Euler equations [24]. The variation of the cost function consists of two terms, one due to variation of the flow field and the the other due to modification of boundaries. The

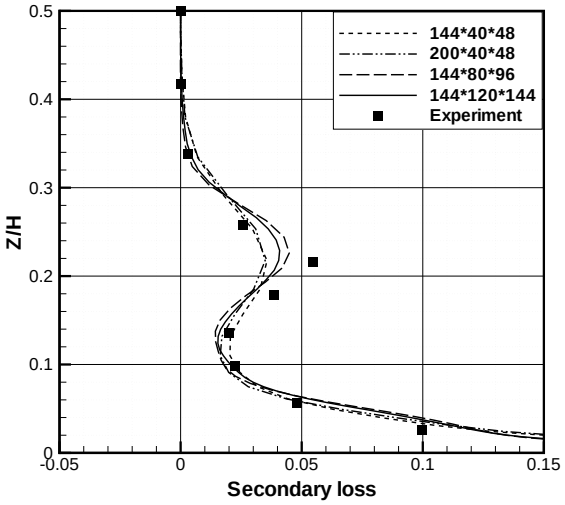

Figure 4. SECONDARY LOSS COMPARISON OF CFD RESULTS AGAINST EXPERIMENTAL DATA

variation of the flow field δW depends implicitly on the variation of the geometry $\delta\mathcal{F}$ through the Navier-Stokes equations. Following the approach by Jameson [15], we multiply the flow equations by a Lagrange multiplier Ψ^T and adding it to the variation of cost function to eliminate the explicit dependence of δI on δW by setting

$$[\frac{\partial I}{\partial W}]^T - [\frac{\partial R}{\partial W}]^T = 0 \tag{11}$$

which is recognized as the adjoint equation. We then have

$$\delta I = G\delta\mathcal{F} \tag{12}$$

where G is the gradient and

$$G = [\frac{\partial I}{\partial \mathcal{F}}] - \Psi^T[\frac{\partial R}{\partial \mathcal{F}}] \tag{13}$$

The optimization problem is then reduced to solving the Navier-Stokes equations and their corresponding adjoint equations to obtain the values of Ψ. The gradient can then be easily and efficiently computed by using Eqn.(13) even for a large number of design parameters because the computational cost depends only on that for the perturbation of geometry. Once the gradient is determined the steepest descent method is used as the optimization algorithm in the present study.

In this paper, the cost function is defined as an integral at the exit cross section. A weak form of the Navier-Stokes equations is

$$\int_D \frac{\partial \Psi^T}{\partial \xi_i}(\delta F_i - \delta F_{vi})dD - \int_B \Psi^T(\delta F_i - \delta F_{vi})dB = 0 \tag{14}$$

where $F_i = S_{ij}f_j$, $F_{vi} = S_{ij}f_{vj}$, and $S_{ij} = JK^{-1}_{ij}$, $K_{ij} = \frac{\partial x_i}{\partial \xi_j}$. Adding Eqn.(14) to the variation of cost function, we have

$$\begin{aligned}\delta I = &\int_{B_o} \delta C dB - \int_B n_i \Psi^T(\delta F_i - \delta F_{vi})dB \\ &+ \int_D \frac{\partial \Psi^T}{\partial \xi_i}(\delta F_i - \delta F_{vi})dD\end{aligned} \tag{15}$$

where C is a scalar function of both flow variables and geometric variables and depends on the definition of the cost function.

The term δC is divided into two terms, δC_f which denotes the flow variation term, and δC_g which denotes the geometry variation term. δC_f can be used to determine the boundary conditions for viscous adjoint equations and thus be eliminated in the cost function. Finally, the variation of cost function can be written in a simplified form:

$$\begin{aligned}\delta I = &\int_{B_{IOF}} [-n_i(\delta S_{ij})\Psi^T f_j + \delta C_g]dB \\ &+ \int_{B_W} [n_i(\delta S_{ij})\psi_k(\sigma_{jk} - p\delta_{jk}) + \delta C_g]dB \\ &+ \delta I_g\end{aligned} \tag{16}$$

where δI_g denotes the variation of cost function due to geometry variation. The subscript IOF denotes the inlet, outlet and far field boundary and W denotes wall boundary. The adjoint equations and gradient formula are given in Appendix A in detail.

In performing the derivations of the adjoint equations of the present study, variations of the viscosity μ and thermal conductivity k including their turbulent contributions are neglected. This is acceptable since we assume the variation of the flow field is small within each design cycle. In addition, we expect the flow to be relatively well-behaved since we are seeking an optimized design so that the dependence of the turbulence eddy viscosity and heat diffusivity on the flow field is relatively weak. Notice, that both the viscosity and thermal conductivity are updated after each design cycle when the Navier-Stokes equations and the turbulence model equations are solved again with the updated geometry. Therefore, the flow solutions will converge with the correct turbulence parameters once the design reaches an optimum.

RESULTS AND DISCUSSION

Three design optimization studies are performed relative to the base reference design geometry. The inlet and outlet bound-

ary conditions are not changed from the base design. All three design cases seek to minimize the entropy increase through the bladerow. The cost function is defined as a combination of entropy generation per unit mass flow rate and a penalty function.

$$I = s_{gen} + \Lambda|\bar{\beta} - \bar{\beta}_0|$$

where $\bar{\beta}$ is the mass-averaged flow turning

$$\bar{\beta} = \frac{\int_{B_O} \rho u_j \beta N_j dA}{\int_{B_O} \rho u_j N_j dA}$$

$\bar{\beta}_0$ is the mass-averaged flow turning of the reference blade and is here selected as the target. β is the flow turning on each cell face at the exit, which is computed as the inverse tangent of the tangential velocity to the axial velocity. A proper value of the coefficient Λ in front of the penalty function must be selected to enforce the exit flow angle constraint.

We first seek improvement by changing the spanwise distribution of the stagger angle of the base blade profile. The approach, however, is found to be of limited benefit for this blade. Therefore, in the second case, we allow modifications in both the stagger angle and the blade profile. Finally, we investigate the effect of end-wall contouring.

A. Re-staggering the Blade Along Span

The stagger angle of each blade section plays an important role in determining the flow turning at the spanwise location and thus the secondary flow loss. We thus seek a spanwise stagger angle distribution of the original two-dimensional blade profile that minimizes the entropy production of the blade row while maintaining the same average exit flow angle of the original base design. There are 49 design parameters, representing the stagger angles of the 49 blade sections in the grid. The coefficient of the penalty function Λ in the cost function is chosen to be 50 for this case. After 20 design cycles of this case, the mass-averaged total pressure at the exit is increased by 0.017%, corresponding to a 0.052% increase in adiabatic efficiency. The average flow turning is kept the same. As expected the secondary loss is decreased by about 3.99%. However, the profile loss of the redesigned blade is increased by about 2.28%.

Figure 5 shows the change of stagger angle distribution along the span. The stagger angle decreases from 5 to 25 percent of the span, while it increases under 5% of the span and near the midspan to ensure the fixed average flow turning. The exit flow angle distributions for both the reference and redesigned blades are shown in figure 6, which are consistent with the variation of stagger angle distribution. Such a stagger angle distribution has the effect of smoothing the loading in the spanwise direction and hence inhibit the generation of secondary flow. The secondary loss of the redesigned blade is noticeably reduced from 5 to 15 percent of the span as shown in Fig. 7.

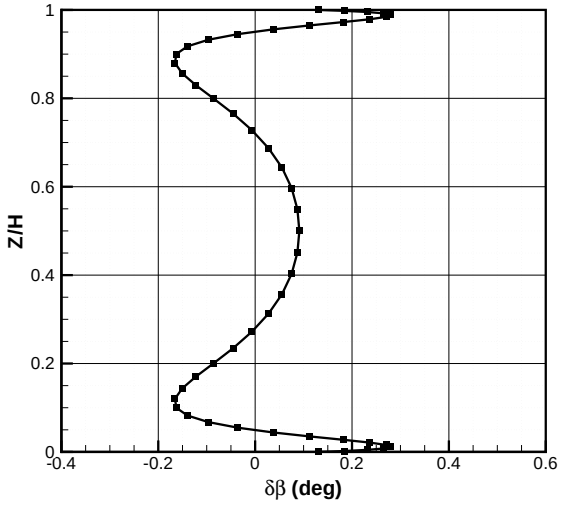

Figure 5. DESIGN CHANGE OF STAGGER ANGLE DISTRIBUTION

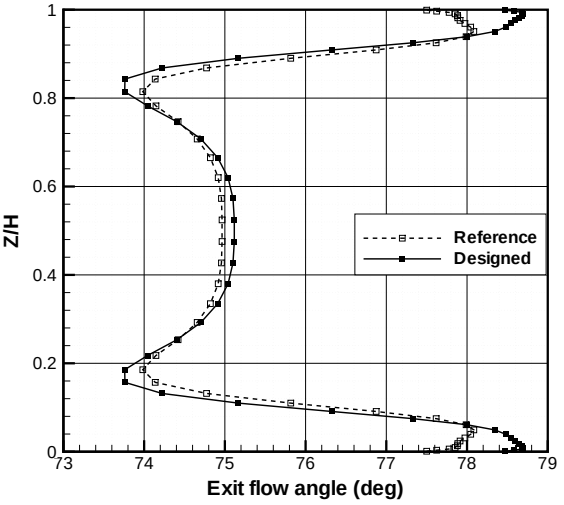

Figure 6. SPANWISE FLOW TURNING DISTRIBUTION

The profile loss is defined on the assumption that the flow at the midspan is regarded as two-dimension. The flow in this blade row is subsonic. Therefore, the profile loss is purely due to viscous losses in the boundary layer over the blade. Increased stag-

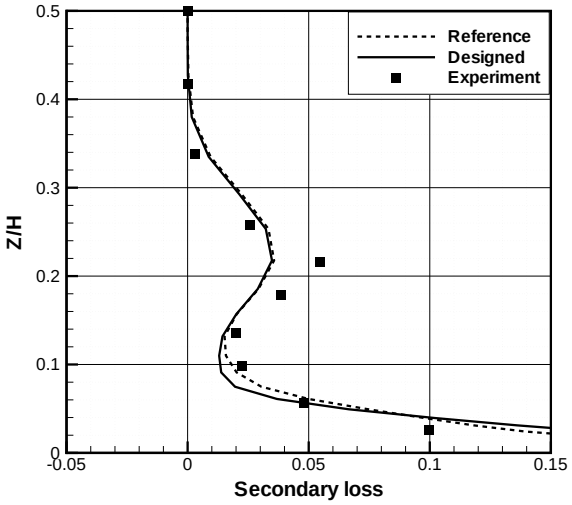

Figure 7. SECONDARY LOSS DISTRIBUTION IN SPANWISE

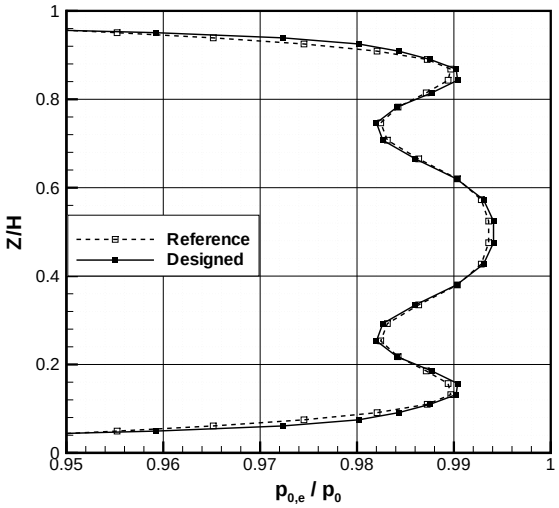

Figure 8. SPANWISE TOTAL PRESSURE DISTRIBUTION

ger angle increases the local loading and thus the flow turning at the given spanwise location. The increased loading increases the profile loss similar to the flow around an airfoil where an increased angle of attack leads to higher flow loss. Figure 8 shows the exit total pressure distribution along the span. The total pressure is slightly decreased at the midspan because of the increased profile loss with the increased local stagger angle. The total pressure across the blade row is increased from 5 to 15 percent of the span because of the reduced secondary loss as shown in figure 7. The reduction of secondary loss more than compensates the increased profile loss, bringing about the slightly improved average total pressure value of the redesigned blade row.

B. Modifying the Blade Shape Combined with Re-staggering

The above subsection demonstrates positive but small gain in performance of the blade row by only re-staggering the blade along span. Similar to a previous work by the present authors [24], the blade can be redesigned with both change of blade profile and re-staggering. Modifying the blade shape can significantly change the loading and therefore the development of the secondary flow. The Hicks-Henne shape functions adopted in our previous work [24] are used to modify the shape of the blade sections. A value of 20 is used for Λ in the cost function.

Figure 9 presents the change of the stagger angle by the redesign. The stagger angle increases from the hub to 5% span and decreases from 5% to 50% span. As in the previous design case, this trend of stagger change reduces the secondary flow loss. Unlike the result of the above case, however, the stagger angle near the mid span of this case is not required to increase on introducing simultaneous modification of the blade profiles. In fact, it decreases near the mid span, resulting potentially reduced profile loss. In order to examine the separate and combined effects of the blade profile change and the stagger angle change, we compute and compare the performances of four blade designs. Blade 1 is the original reference blade; Blade 2 (Designed) is the optimized blade with both the profile change and the restagger; Blade 3 (Shape only) includes only the blade profile change of the redesign without its stagger angle change; Blade 4 (Stagger), however, has the stagger angle change of the optimized blade (Blade 2) without its shape change;

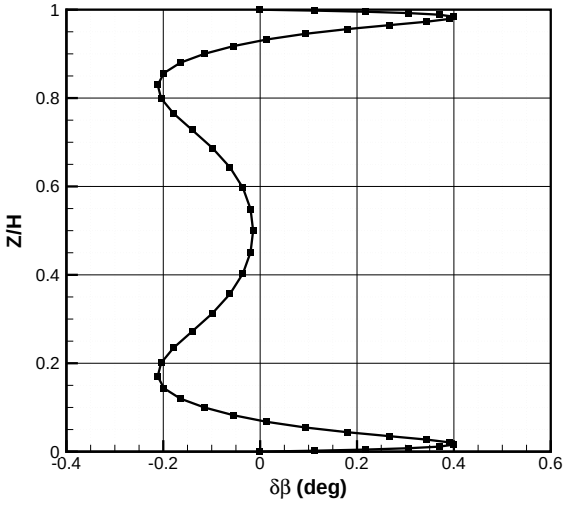

Figure 9. DESIGN CHANGE OF STAGGER ANGLE DISTRIBUTION

Figure 10 shows the exit flow turning distribution of the four different blades. Compared to the reference blade, The stagger angle change increases the exit flow angle in a narrow region between the hub and about 20% blade height, but increases the flow angle in the larger mid-height range, resulting in an increased average exit flow angle. In order to satisfy the fixed average exit flow angle condition, the shape modifications has the effect of decreasing flow angle from hub to 20% span and increasing it from 20% to mid span.

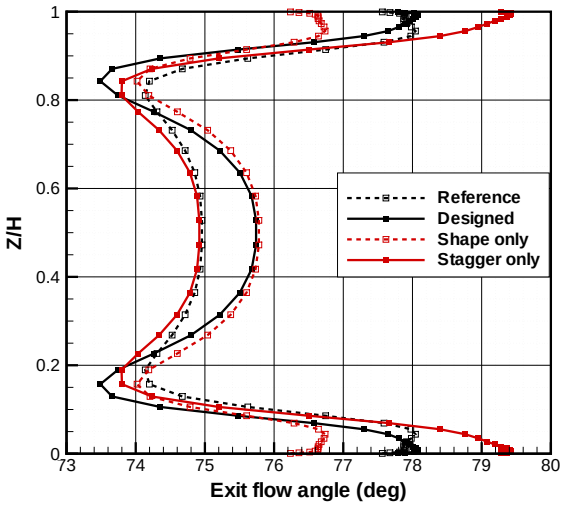

Figure 10. SPANWISE FLOW TURNING DISTRIBUTION

Figure 11 presents the secondary flow loss distributions along the span. Figure 12 plots the exit total pressure of the four blades. The breakdown of the different losses for the four blades are listed in Table 3. Both the blade shape modifications and stagger angle change reduce the secondary flow loss, bringing about a significant combined reduction of the secondary flow loss by the re-designed blade. The stagger change slightly reduces the profile loss because of the overall reduced flow angle. The profile file change, however, increases the profile loss in the process of bringing back the exit flow angle to satisfy the constraint. The combined effect still increases the profile loss, but is compensated by the larger improvement in secondary flow loss. Overall, a 2.33% reduction in total pressure loss compared to the reference blade is achieved with the combined optimization.

Figure 13 presents the isentropic Mach number on the blade surface at 10%, 20%, and 30% of blade height. Compared to that for the reference blade, the loading of the redesigned blade is decreased from 20% to 55% axial chord in all of the three spanwise stations. At the 20% and 30% of blade heights, the loading increases from the leading edge to about 20% axial chord because

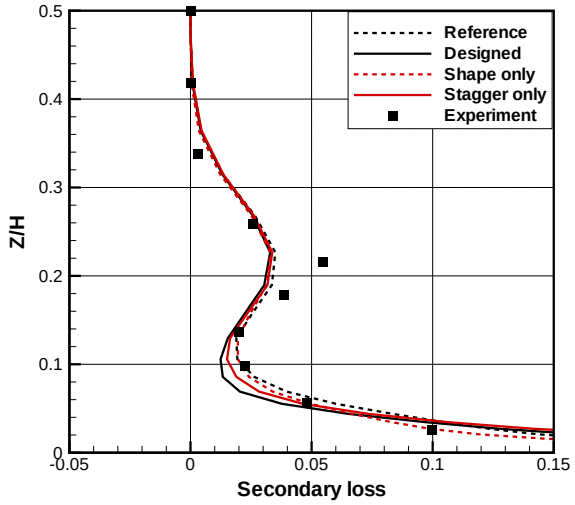

Figure 11. SECONDARY LOSS DISTRIBUTION IN SPANWISE

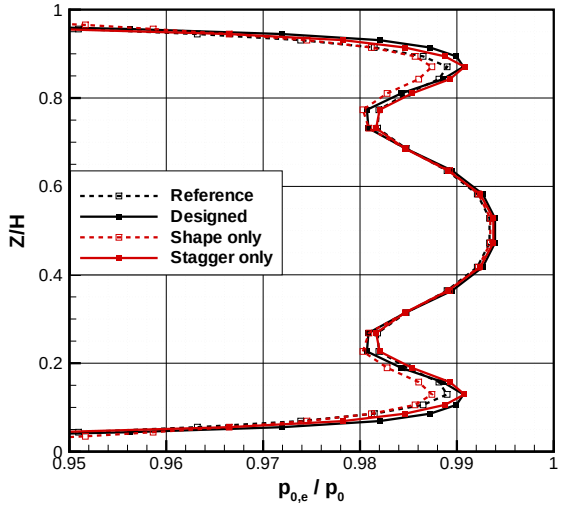

Figure 12. SPANWISE TOTAL PRESSURE DISTRIBUTION

of the larger suction on the suction surface, and then again from 55% axial chord to the trailing edge due to the increased pressure on the pressure surface. At the 10% height near the end wall, however, the redesigned blade reduces loading in the 20% to 60% axial chord range without increasing loading in other parts of the blade length. The reduced loading means a smaller pressure gradient near the end walls and therefore inhibits the generation of secondary flow and consequently reduces the secondary loss. Table 4 and Table 5 list the secondary and total losses, respectively, at the 50%, 100%, and 150% axial chord locations from the leading edge for the reference and the redesigned blades. At 50% axial chord, the secondary loss is reduced by 11.3% because of

Table 3. THE EFFECTS OF STAGGER AND BLADE SHAPE TO FLOW

Blade	1	2	3	4
p_0	0.98153	0.98199	0.98132	0.98211
β (deg)	75.1095	75.1398	75.2776	74.9834
ζ_0 (%)	3.91191	3.82079	3.92877	3.79726
ζ_p (%)	2.01999	2.11563	2.17037	2.01264
ζ_s (%)	1.89192	1.70517	1.75840	1.78462

the reduced sectional loading near the end walls. However, the reduced loading resulted reduced flow turning, which must be compensated by increased loading away from the end walls, giving rise to increase profile loss. The total loss decreases for the designed blade except at the location of 50% axial chord. At this location, the secondary loss decreases due to the reduced pressure gradient in the pitchwise direction. However, the profile loss increases due to the increased loading at mid-span. As the flow goes further downstream, the reduction in secondary flow loss catches up with the increase of profile loss.

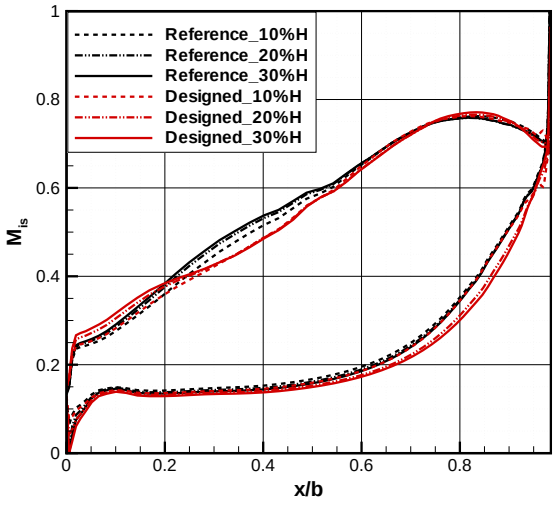

Figure 13. ISENTROPIC MACH NUMBER DISTRIBUTION ON BLADE SURFACE

Table 4. Secondary loss (%) at three different axial locations

Locations	50%	100%	150%
Reference	0.30492	0.72224	1.89192
Designed	0.27034	0.55722	1.70517

Table 5. Total loss (%) at three different axial locations

and

Locations	50%	100%	150%
Reference	1.98375	2.68232	3.91191
Designed	2.13722	2.65578	3.82079

C. Endwall Contouring

For low aspect ratio blades, the secondary loss involves a considerable part of the total loss. Much research has already shown that non-axisymmetric contouring of the endwall profile is effective in reducing the secondary loss. The basic mechanism is to modify the pressure gradient in the pitchwise direction, as discussed by Dossena [11] and Sonoda [3]. This test case demonstrates the use of the optimization method in determining the best end wall contours for the given flow conditions. No blade shape nor stagger angle changes are considered at present. The value of Λ in the cost function is 5 for this case.

Perturbations are added on the base endwall contours in the form of a Fourier summation of 4 harmonics:

$$\delta z(x,s) = \sum_{i=1}^{4} [A_i(x) sin(i\pi \frac{s}{s_0}) + B_i(x) cos(i\pi \frac{s}{s_0})] + C(x) \quad (17)$$

where s_0 is the local pitch. Compared with the perturbation adopted by Corral [26], an equivalent perturbation is not required for the blade surfaces and consequently there are more potential profiles for the redesigned endwalls. The endwall contours are applied symmetrically at the hub and casing for this linear cascade test case.

Figure 14 shows the total pressure and entropy generation of the blade row versus design cycles. Within 16 design cycles, the total pressure increases by about 0.09 of a percentage point. Figure 15 shows that the exit flow angle keeps very close to that of the reference blade and the maximum difference is only 0.04 degree. It means that the constraint is strictly enforced in the design process. The mass flow rate, however, is increased by about 0.25 of a percentage point due to the reduced loss and thus viscous blockage. This is an added benefit of the optimized blade row.

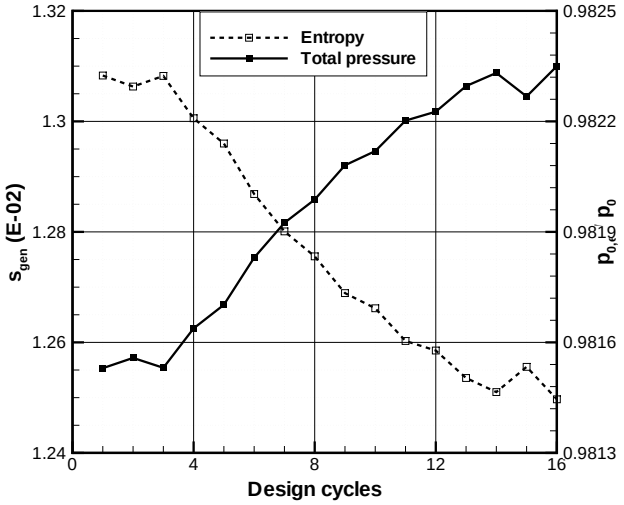

Figure 14. TOTAL PRESSURE AND ENTROPY VS. DESIGN CYCLES

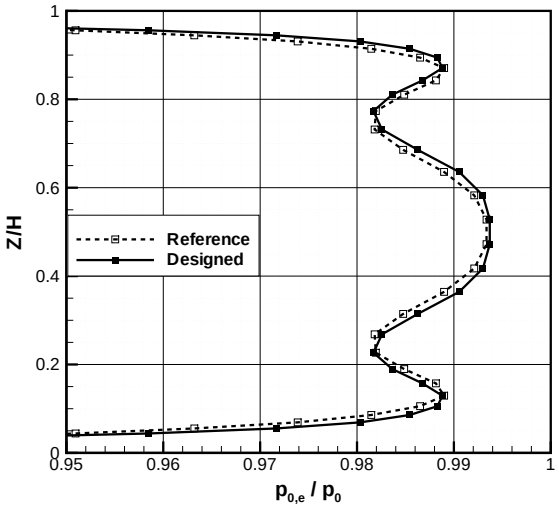

Figure 16. SPANWISE TOTAL PRESSURE DISTRIBUTION

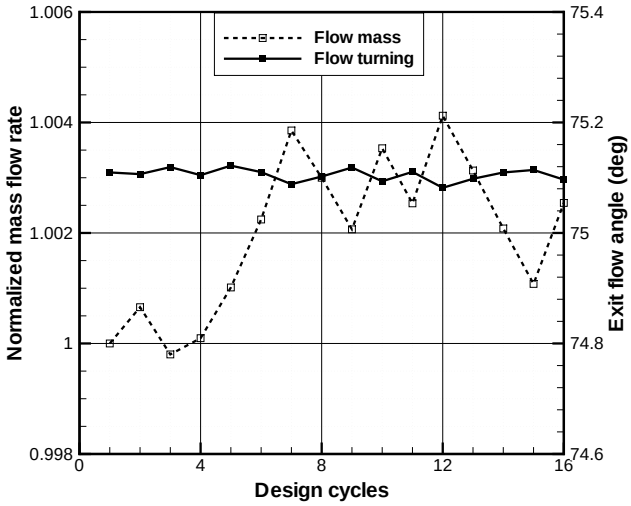

Figure 15. TURNING ANGLE AND FLOW MASS VS. DESIGN CYCLES

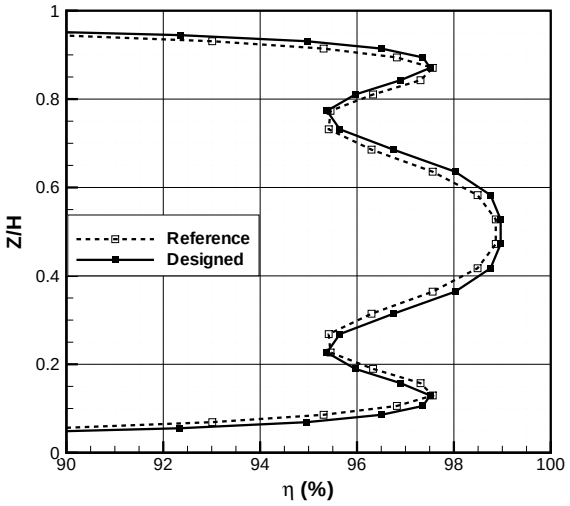

Figure 17. SPANWISE ADIABATIC EFFICIENCY DISTRIBUTION

Figure 16 and figure 17 show the total pressure and adiabatic efficiency distributions in the spanwise direction for both the reference and designed blades at the outlet plane. The total pressure of the designed blade increases at the spanwise locations from 5 to 10 percent and from 25 to 50 percent. Notice that the total pressure of the designed blade remains nearly the same at the midspan. This implies that the profile loss is the same as that of the reference blade. Figure 18 shows the exit flow angle distributions along the span at the outlet. The exit flow angle is decreased from 5 to 20 percent but is increased in the rest of the blade height to maintain an unchanged average exit flow angle.

Figure 19 shows the secondary loss distribution along the span. Compared with the reference blade, the secondary vortex of the redesigned blade migrates to the endwalls and the secondary loss decreases on the blade sections where the designed total pressure increases as presented in figure 16.

Figure 20 shows the three dimensional contoured endwall profile of the hub from the leading edge to the trailing edge. Figure 21 shows the modified endwall profile on five different specified pitchwise locations. The J=01 line corresponds to the pressure surface, while the J=41 line corresponds to the suction surface of the blade. The other grid lines are distributed in the

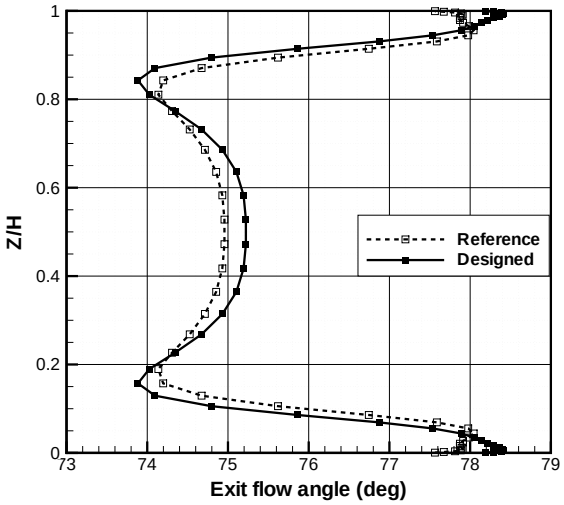

Figure 18. SPANWISE FLOW TURNING DISTRIBUTION

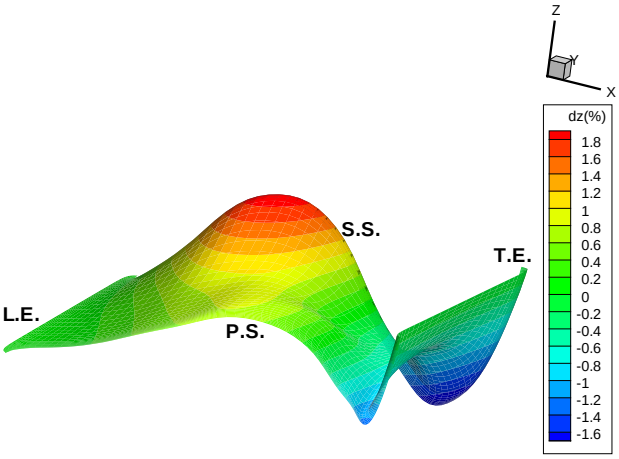

Figure 20. 3-D CONTOURED ENDWALL PROFILE

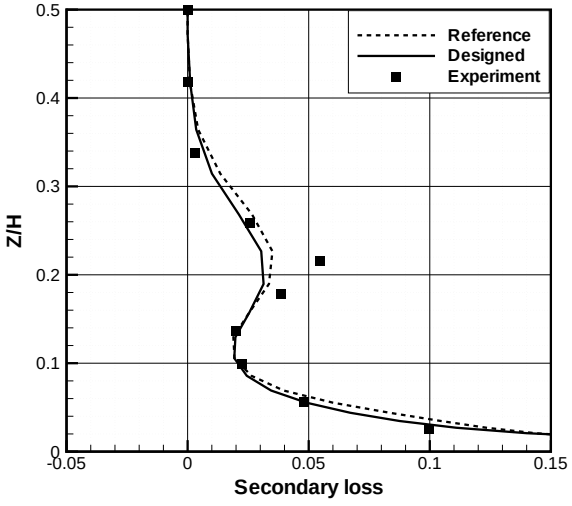

Figure 19. SECONDARY LOSS DISTRIBUTION IN SPANWISE

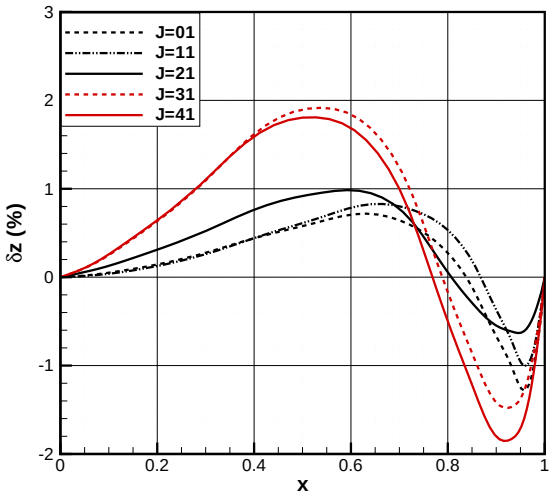

Figure 21. CONTOURED ENDWALL PROFILE AT SPECIFIED PITCH-WISE LOCATIONS

flow passage between the pressure and suction surfaces. The effect of the endwall contouring results in an effective converging-diverging channel for the flow passage between the blades. The channel convergence accelerates the flow from the leading edge to the mid chord station. After that point, the flow is decelerated because of the channel divergence. In the circumference direction, the endwall profile near the suction side is contoured upward from leading edge to mid chord, while it is contoured downward on the rear portion. Such a modification of endwall profile leads to reduced cross-passage pressure gradient towards the trailing edge. As shown in figure 22, the pressure gradient in the pitchwise direction increases from 30% to 70% of axial chord on the hub, while it decreases from 70% of axial chord to the trailing edge. The reduction of secondary flow loss might be argued by the fact that the endwall contouring increases front load on the blade where the endwall boundary layer is still thin but increases the loading in the rear part of the passage where the endwall boundary layer becomes thicker. The influence of contoured endwalls weakens as one moves towards the mid span. The loading at 5% span of the redesigned blade is closer to that of the reference blade.

In order to visualize the development of the secondary flow

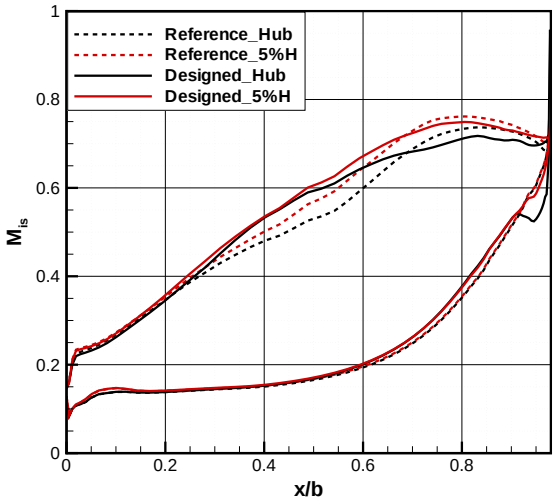

Figure 22. ISENTROPIC MACH NUMBER DISTRIBUTION ON BLADE SURFACE

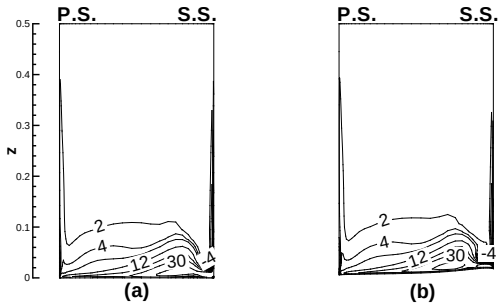

Figure 23. CONTOURS OF VORTICITY AT 50% AXIAL CHORD

for both the reference and designed blades, the contours of streamwise vorticity and secondary loss in the planes located at three different axial locations are presented in the following pictures. These planes are normal to the axial direction. Figure 23 and figure 24 present the contours on the planes located at 50% axial chord for both the reference. The subfigures (a) and (b) are for the reference and the redesigned cases, respectively. *P.S.* and *S.S.* in the figures denote the pressure and suction sides, respectively. The positive vorticity in figure 23 identifies the passage vortex, while the negative vorticity identifies the suction-side leg of the horseshoe vortex, which is usually swept by passage vortex [10]. The size and strength of passage vortex for the redesigned blade are almost the same as those of the reference blade. In figure 24, the peak value of the secondary loss for the redesigned blade is slightly increased compared with that of the reference blade. However, as previously defined, the secondary loss is referenced to the flow loss at the midspan. In reality, from the results listed in Table 6, the secondary loss is slightly reduced for the redesigned blade and the reduction is mainly contributed by the acceleration of the flow.

Figure 25 and figure 26 present the contours on the planes located at the trailing edge, where the contoured endwall profile is blended back to the original shape. The secondary flow is fully developed at this location. The passage vortex moves toward the suction side along with the cross flow in the boundary layer and totally sweeps the horseshoe vortex. From figure 25, the passage vortex migrates toward the endwall and the size is reduced for the redesigned blade. The reduced pressure gradient in the pitchwise direction, corresponding to the deceleration of the flow contributes to the reduction of secondary flow. As shown in

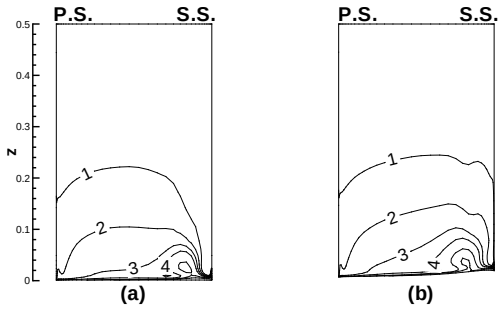

Figure 24. CONTOURS OF SECONDARY LOSS AT 50% AXIAL CHORD

figure 26, the peak value of secondary loss is much less and the secondary flow is significantly confined. As shown in Table 6, the secondary loss for the redesigned blade decreases by about 19.8%.

Figure 27 and figure 28 present the contours on the planes located at 150% axial chord, which is the measurement location in the experiments. Since it is far away from the trailing edge, the secondary kinetic energy has been considerably dissipated at this location. As shown in figure 27, the strength of the passage vortex for both the reference and designed blades decreases. However, the size of the passage vortex of the redesigned blade is still reduced, compared with that of the reference blade. The

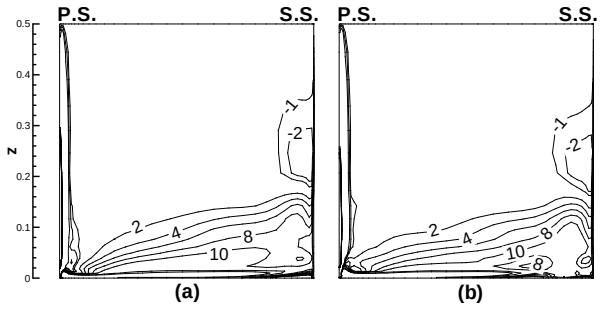

Figure 25. CONTOURS OF VORTICITY AT TRAILING EDGE

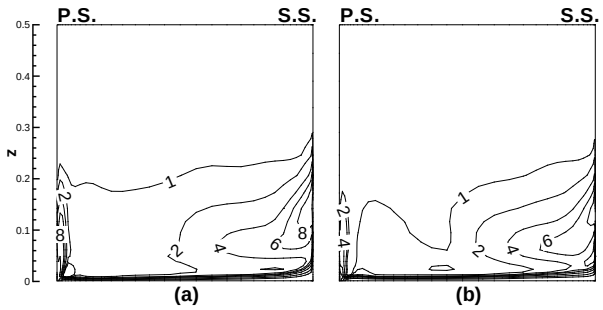

Figure 26. CONTOURS OF SECONDARY LOSS AT TRAILING EDGE

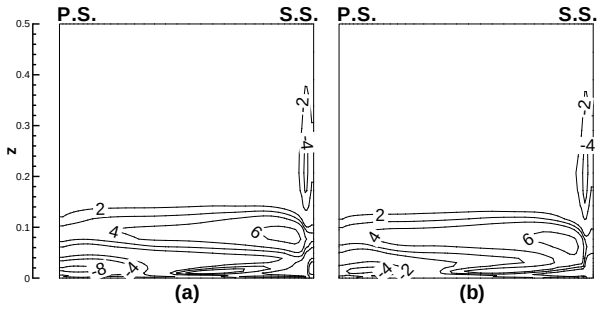

Figure 27. CONTOURS OF VORTICITY AT 150% AXIAL CHORD

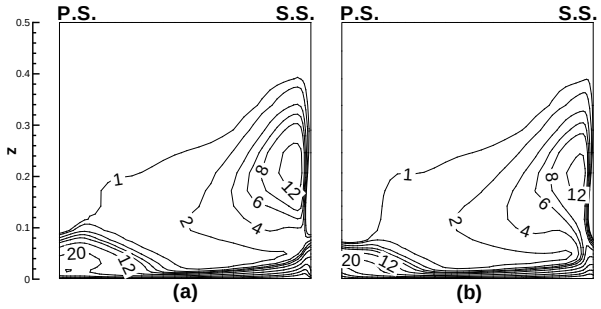

Figure 28. CONTOURS OF SECONDARY LOSS AT 150% AXIAL CHORD

vortex identified by the negative vortictity and located above the passage vortex originates from the trailing edge and is named as the trailing shed vorticity [10] or it is originates from the suction side and is named as the wall induced vortex [27]. In this design case, it is difficult to reduce the strength of this vortex. There is only a little improvement in vortex size and strength for the redesigned blade. The two cores indentified by the negative vorticity and located near the endwall are recognized as the corner vortices, which extend in both pitchwise and spanwise directions. The strength of these vortices are significantly decreased for the redesigned blade. At the measurement location, the secondary loss decreases by about 11.7% as shown in Table 6.

Table 7 presents the total pressure loss at the selected three different axial locations. The reduction of the total loss, which consists of mainly profile loss and secondary loss, at all the three locations show that the contoured endwall profiles can effectively confine the secondary flow with the constraint on flow turning.

CONCLUSION

A continuous adjoint method based on the Navier-Stokes equations is presented for the aerodynamic design optimization

Table 6. Secondary loss (%) at three different axial locations

Locations	50%	100%	150%
Reference	0.30492	0.72224	1.89192
Designed	0.20561	0.57925	1.67061

Table 7. Total loss (%) at three different axial locations

Locations	50%	100%	150%
Reference	1.98375	2.68232	3.91191
Designed	1.84981	2.57003	3.68803

of turbomachinery blade rows. Gradient information of the cost function is obtained by solving the Navier-Stokes equations and their corresponding adjoint equations only once, independent of the number of design parameters. A base flow solver incorporates the *k*-ω SST turbulence model uses a third order Roe scheme for the Euler part of the equations. A scalable wall function method is implemented in order to relieve the stringent grid requirement near walls. The flow solver with the use of the wall function is validated for the turbulent flow over a flat-plate and also for the flow through the linear cascade under consideration for optimizatin by comparing the computed profile and secondary flow losses with measured data from experiments and the solutions on successively finer grids with and without the wall function. Optimization studies are performed on a grid that shows near grid independent solutions.

Three design optimization cases are performed with the common objective of minimizing entropy production through the blade row while maintaining a fixed average turning angle. The first design cases attempts to do so by restaggering the original blade profile in the spanwise direction. An optimal spanwise distribution of the blade stagger angle is determine, which gives a slight reduction in the overall total pressure loss. The optimization attempts to reduce the turning in the near wall region but increases turning at the mid-span in order to maintain the same average exit flow angle. The over-turning in the mid-span region increases the profile loss, but for this low-aspect ratio blade, the reduction in secondary flow due to restaggering dominates and therefore brings about a positive gain on overall efficiency.

The second design case allows changes both in stagger angle and blade profiles. The separate and combined effects of the stagger angle and blade profile changes are investigate. The stagger angle changes of the redesigned blade is responsible for a large portion of the reduction in secondary flow loss, but it reduces the overall turning angle of the flow. The modification of the blade shape, however, counter-acts the flow turning changes due to restagger. In addition, the shape modification decreases the loading near the hub and hence inhibit the generation of secondary flow. The combined effect of the restagger and profile change significantly reduces the secondary flow loss with only a small increase in profile loss.

Finally, optimization by using endwall contouring is studied for this blade row. The automatic design optimization code produces a three-dimensional endwall shape that raises the endwall near the suction side of the blade before mid chord but lowers it after the mid chord position. This has the dual effect of accelerating the flow and increasing the pitchwise pressure gradient in the front portion of the blade passage while doing the opposite in the after portion of the passage. The reduction in secondary flow loss is achieved by incresing flow turning when the endwall boundary layer is still thin and the flow speed is high and then reducing the turning in the rear part of the blade where the endwall boundary layer is thick and flow speed is low.

ACKNOWLEDGMENT

The authors would like to thank Alstom Power for support this research work through a research contract to UCI. The first author also received support from China Scholarship Council for his studies at UCI.

REFERENCES

[1] Samad, A., and Kim, K. Y., 2008. "Multiple surrogate modeling for axial compressor blade shape optimization". *Journal of Propulsion and Power*, **24**(2).

[2] Jang, C. M., Li, P., and Kim, K. Y., 2005. "Optimization of blade sweep in a transonic axial compressor rotor". *JSME International Journal*, **48**(4).

[3] Sonoda, T., Hasenjager, M., Arima, T., and Sendhoff, B., 2009. "Effect of end wall contouring on performance of ultra-low aspect ratio transonic turbine inlet guide vanes". *Journal of Turbomachinery*, **131**(1).

[4] Hager, J. O., Eyi, S., and Lee, K. D., 1993. Design efficiency evaluation for transonic airfoil optimization:a case for navier-stokes design. AIAA Paper 93-3112.

[5] Wilcox, D. C., 2001. Turbulence modeling: An overview. AIAA Paper 2001-0724.

[6] Kalitzin, G., Medic, G., Iaccarino, G., and Durbin, P., 2005. "Near-wall behavior of rans turbulence models and implications for wall functions". *Journal of Computational Physics*, **204**.

[7] Shih, T. H., Povinelli, L. A., Liu, N. S., Potapczuk, M. G., and Lumley, J. L., 1999. A generalized wall function. NASA/TM 209398.

[8] Horlock, J. H., and Lakshminarayana, B., 1973. "Secondary flows: Theory, experiment, and application in turbomachinery aerodynamics". *Annual Review of Fluid Mechanics*, **5**.
[9] Perdichizzi, A., 1990. "Mach number effects on secondary flow development downstream of a turbine cascade". *Journal of Turbomachinery*, **112**(4).
[10] Perdichizzi, A., and Dossena, V., 1993. "Incidence angle and pitch-chord effects on secondary flows downstream of a turbine cascade". *Journal of Turbomachinery*, **115**(3).
[11] Dossena, V., Perdichizzi, A., and Savini, M., 1999. "The influence of endwall contouring on the performance of a turbine nozzle guide vane". *Journal of Turbomachinery*, **121**(2).
[12] Dossena, V., D'Ippolito, G., and Pesatori, E., 2004. Stagger angle and pitch-chord ratio effects on secondary flows downstream of a turbine cascade at several off-design conditions. ASME Paper GT2004-54083.
[13] Koiro, M., and Lakshminarayana, B., 1998. "Simulation and validation of mach number effects on secondary flow in a transonic turbine cascade using a multigrid, *k*-ε solver". *Journal of Turbomachinery*, **120**(2).
[14] Hermanson, K. S., and Thole, K. A., 2000. "Effect of inlet condition on endwall secondary flows". *Journal of Propulsion and Power*, **16**(2).
[15] Jameson, A., 2003. Aerodynamic shape optimization using the adjoint method. Lectures at the von karman institute.
[16] Jameson, A., 1988. "Aerodynamic design via control theory". *Journal of Scientific Computing*, **3**(3).
[17] Jameson, A., 1995. Optimum aerodynamic design using cfd and control theory. AIAA Paper 95-1729.
[18] Kim, S., Alonso, J. J., and Jameson, A., 2004. "Multi-element high-lift configuration design optimization using viscous continous adjoint method". *Journal of Aircraft*, **41**(5).
[19] Yang, S., Wu, H., and Liu, F., 2003. Aerodynamic design of cascades by using an adjoint equation method. AIAA Paper 2003-1068.
[20] Wu, H., and Liu, F., 2005. Aerodynamic design of turbine blades using an adjoint equation method. AIAA Paper 2005-1006.
[21] Papadimitriou, D. I., and Giannakoglou, K. C., 2006. A continuous adjoint method for the minimization of losses in cascade viscous flows. AIAA Paper 2006-49.
[22] Wang, D., and He, L., 2008. Adjoint aerodynamic design optimization for blades in multi-stage turbomachines: Part i-methodology and verification. ASME Paper GT2008-50208.
[23] Wang, D., He, L., Wells, R., and Chen, T., 2008. Adjoint aerodynamic design optimization for blades in multi-stage turbomachines: Part ii-validation and application. ASME Paper GT2008-50209.
[24] Luo, J., Xiong, J., Liu, F., and McBean, I., 2009. Three-dimensional aerodynamic design optimization of a turbine blade by using an adjoint method. ASME Paper GT2009-60115.
[25] Wilcox, D. C., 1998. *Turbulence Modeling for CFD*. DCW Industries, Inc.
[26] Corral, R., and Gisbert, F., 2008. "Profiled end wall design using an adjoint navier-stokes solver". *Journal of Turbomachinery*, **130**(2).
[27] Benner, M. W., Sjolander, S. A., and Moustapha, S. H., 2004. "The influence of leading edge geometry on secondary losses in a turbine cascades at the design incidence". *Journal of Turbomachinery*, **126**(2).

Appendix A: Boundary Conditions, Adjoint Equations and Variation of Cost Functions

Boundary Conditions of Flow Solver

Inlet boundary conditions:

The total pressure p_0, total temperature T_0, the two inflow angles are specified.

Outlet boundary conditions:

The back pressure p is specified.

Viscous Wall boundary conditions:

The velocity on the viscous wall is zero:

$$u_1 = 0, \quad u_2 = 0, \quad u_3 = 0$$

Periodic boundary conditions:

$$w_{i,B2} = w_{i,B1}, \quad i = 1,2,5$$

$$w_{3,B2} = w_{3,B1}cos\theta - w_{4,B1}sin\theta$$

$$w_{4,B2} = w_{3,B1}sin\theta + w_{4,B1}cos\theta$$

where $B1$ and $B2$ are two periodic boundaries; and θ is the pitch angle of annular cascade. For a linear cascade blade, $\theta = 0$

Adjoint Equations

The final expression of the adjoint equations in unsteady form is

$$\frac{\partial \Psi}{\partial t} - A_i^T \frac{\partial \Psi}{\partial x_i} - [M^{-1}]^T \frac{Y}{J} = 0 \tag{18}$$

where $Y = \bar{L}\Psi$ and $\bar{L}$ is the primitive adjoint operator. M is the transformation matrix because the variation of viscous stresses

depend on the velocity gradient $\frac{\partial u_i}{\partial x_j}$ and a transformation to primitive variables must be introduced.

$$\delta\bar{W} = M^{-1}\delta W \tag{19}$$

$$[M^{-1}]^T = \begin{Bmatrix} 1 & -\frac{u_1}{\rho} & -\frac{u_2}{\rho} & -\frac{u_3}{\rho} & \frac{(\gamma-1)u_iu_i}{2} \\ 0 & \frac{1}{\rho} & 0 & 0 & -(\gamma-1)u_1 \\ 0 & 0 & \frac{1}{\rho} & 0 & -(\gamma-1)u_2 \\ 0 & 0 & 0 & \frac{1}{\rho} & -(\gamma-1)u_3 \\ 0 & 0 & 0 & 0 & \gamma-1 \end{Bmatrix} \tag{20}$$

$$Y = J\begin{Bmatrix} -\frac{a^2\mu}{(\gamma-1)P_\gamma\rho}\frac{\partial^2\theta}{\partial x_j^2} \\ \frac{\partial}{\partial x_j}[\mu(\frac{\partial\phi_i}{\partial x_j}+\frac{\partial\phi_j}{\partial x_i})+\lambda\delta_{ij}\frac{\phi_k}{\partial x_k}] \\ +\frac{\partial}{\partial x_j}[\mu(u_i\frac{\partial\theta}{\partial x_j}+u_j\frac{\partial\theta}{\partial x_i})+\lambda\delta_{ij}u_k\frac{\partial\theta}{\partial x_k}]-\sigma_{ij}\frac{\partial\theta}{\partial x_j} \\ \frac{a^2\mu}{(\gamma-1)P_\gamma\rho}\frac{\partial^2\theta}{\partial x_j^2} \end{Bmatrix} \tag{21}$$

where

$$\sigma_{ij} = \mu(\frac{\partial u_i}{\partial x_j}+\frac{\partial u_j}{\partial x_i})+\lambda\delta_{ij}\frac{\partial u_k}{\partial x_k}$$

Inlet and Outlet Boundary Conditions of Adjoint Equations

Since the cost function is selected as the same as that in the paper of present authors [24], the inlet and outlet boundary conditions are the same.

Viscous Wall Boundary Conditions

$$\phi_k = 0, \quad k = 1,2,3 \tag{22}$$

Resultant Variation of Cost Functions due to Geometry Variation

$$\begin{aligned} \delta I_g = & \int_D \frac{\partial\Psi^T}{\partial\xi_i}(\delta S_{ij})(f_j - f_{vj})dD \\ & - \int_D kS_{ij}\frac{\partial\theta}{\partial\xi_i}\delta(\frac{S_{lj}}{J})\frac{\partial}{\partial\xi_l}(\frac{p}{\rho R})dD \\ & - \int_D S_{ij}(\frac{\partial\phi_l}{\partial\xi_i}+\frac{\partial\theta}{\partial\xi_i}u_l)(\delta\sigma^*_{jl})dD, \quad l = 1,2,3 \end{aligned} \tag{23}$$

where

$$\delta\sigma^*_{jl} = \mu\{\delta(\frac{S_{kj}}{J})\frac{\partial u_l}{\partial\xi_k}+\delta(\frac{S_{kl}}{J})\frac{\partial u_j}{\partial\xi_k}\}+\lambda\delta_{jl}\delta(\frac{S_{km}}{J})\frac{\partial u_m}{\partial\xi_k}$$

$$f_j = \begin{Bmatrix} \rho u_j \\ \rho u_1u_j + p\delta_{j1} \\ \rho u_2u_j + p\delta_{j2} \\ \rho u_3u_j + p\delta_{j3} \\ \rho u_jE \end{Bmatrix}, \quad f_{vj} = \begin{Bmatrix} 0 \\ \sigma_{ij}\delta_{i1} \\ \sigma_{ij}\delta_{i2} \\ \sigma_{ij}\delta_{i3} \\ u_i\sigma_{ij}+k\frac{\partial T}{\partial x_j} \end{Bmatrix}$$